Journal of Physics and Chemistry of Solids 150 (2021) 109801

Contents lists available at ScienceDirect

Journal of Physics and Chemistry of Solids

journal homepage: http://www.elsevier.com/locate/jpcs

Band engineering of non-hexagonal 2D tetragonal-silicene sheet and nanoribbons: A theoretical approach

Niladri Sekhar Mondal [a], Subhadip Nath [b,*], Debnarayan Jana [c], Nanda Kumar Ghosh [d]

[a] Department of Physics, Haldia Government College, Haldia, 721657, India
[b] Department of Physics, Krishnagar Government College, Krishnagar, 741101, India
[c] Department of Physics, University of Calcutta, 92 A. P. C. Road, Kolkata, 700009, India
[d] Department of Physics, University of Kalyani, Kalyani, 741235, India

ARTICLE INFO

Keywords:
Density functional theory(DFT)
Tight-binding model
2D materials
Electronic properties
Nanoribbons

ABSTRACT

We report combined first-principle and tight-binding (TB) calculation to investigate the mechanical and electronic properties of non-hexagonal two-dimensional (2D) tetragonal-silicene (TS) sheet and nanoribbons (NRs). The results obtained by the TB method are consistent with the density functional theory (DFT) results. The elastic constants of the TS sheet are comparable to silicene. The existence of two Dirac cones is observed at different $\vec{k}$ points in the irreducible Brillouin Zone. A spin-orbit bandgap larger than silicene is observed in TS. The criteria for the stability and robustness of the Dirac Cones on the TB parameters are extensively investigated. Both the Dirac points are robust and stable under a wide range of hopping parameters. The degeneracy of the Dirac cones can be removed by introducing asymmetry in the on-site energy. Comparing the DFT and TB band structures, the values of the TB hopping parameters are estimated. The electronic properties of the TSNRs show a strong dependence on the width and the edge states. The symmetric armchair TSNRs show a width dependent multiple Dirac cones in the Brillouin zone. The number of Dirac cones of the NR is found to be dependent on the TB hopping parameters as well. On the other hand, asymmetric armchair TSNRs are semiconducting. The tuning of the bandgap for asymmetric armchair TSNRs by modulating the TB hopping parameters is also explored. Zigzag TSNR behaves as a degenerate semiconductor with the presence of Dirac cones just below and above E_F. We subsequently expect that these theoretical findings will give a better comprehension of Dirac materials and their NRs with its potential application in nano-electronics.

1. Introduction

The discovery of graphene [1] has attracted enormous research interests, both theoretically and experimentally, due to its conceivable application in electronics, photonics, opto-electronics, thermoelectric application, etc. [2–5]. This lies in the graphene's inherent extraordinary properties regarding robustness, flexibility, stability, electrical, thermal conductivity, half-integer quantum hall effect etc. [1,6,–9]. One of the potential grips for explaining these amazing properties of graphene is its special band structure (BS) with highlighting Dirac points and cones. Descending through the other group-IV elements, the 2D structure of silicon (silicene), germanium (germanene), tin (Stanene), and their electronic properties have also got immense consideration [10–14]. The low-buckled honeycomb lattice silicene and germanene, an analog of graphene with two atoms per unit cell are the two reported structures [10,11] having linear dispersion relation near Fermi energy.

Silicene is unstable in planar structure, but alternate atom slightly buckled in z-direction gives a stable structure. Again, free-standing silicene is unstable in the air and hence a substrate is needed for epitaxial growth of silicene due to its tendency toward sp^3 hybridization. Hence, in experiments silicene is synthesized in substrates like Ag(111), Ir(111), etc. [15,16], but this destroys the Dirac Fermion characteristics of silicene and reduces the carrier mobility. Still, silicene remains one of the emerging 2D materials with a similar Dirac physics like graphene, but with a larger spin-orbit coupling inducing a bandgap of 1.55 meV at the K point [17]. Contrary to graphene, silicene also has an intrinsic spin-orbit coupling, which plays a significant role in spin transport [18]. Therefore, silicene has the opportune both in principle and analyses because of its potential applications in the current Si-based industry.

The electronic, optical and other properties of the 2D materials

* Corresponding author.
E-mail address: subha.31connect@gmail.com (S. Nath).

https://doi.org/10.1016/j.jpcs.2020.109801
Received 31 July 2020; Received in revised form 8 September 2020; Accepted 9 October 2020
Available online 15 October 2020

including graphene and silicene can be tuned, for implementation in nanodevices, by tailoring the 2D materials into nanoribbons (NRs), nanodots with edges, and/or by chemical functionalization. For example, graphene NRs (GNRs) are either metal or semiconductor depending on ribbons width and edge orientation [19–21]. The electronic and optical properties of silicene NRs (SiNRs) also exhibit important electronic properties based on the edge geometry and width. For example, the bandgap of armchair SiNRs (ASiNRs) oscillates with a period of three with the increase of NR width [22–24]. Again similar to zigzag GNRs, the bandgap of zigzag SiNRs (ZSiNR) decreases monotonically with the increase of width [23]. A symmetry dependent transport property is also observed for ZSiNRs [25]. In Ref. [26], the authors also reported the magnetic properties of planar silicene by introducing a defect/doping. SiNRs are found to be promising materials for future nanodevices such as FET and gas sensor [27].

Nevertheless, these methodologies have not been sufficiently improved concerning their proficiency in a realistic application in nanoscience and nanotechnology. Thus, an inquiry of new allotropes of graphene, silicene is of intrigue. Initially, it was suggested that hexagonal symmetry is one of the essential conditions for the emergence of Dirac cones. But, there are some 2D graphene allotropes which possess Dirac cones without hexagonal symmetry [28–31]. Non-hexagonal allotropes like 6,6,12-graphyne and S-graphene (SG) possess two Dirac cones in their irreducible Brillouin zone (IBZ) and are more versatile than the hexagonal graphene. The robustness and the stability of the two Dirac cones of SG and 6,6,12 graphyne are explored by using a tight-binding (TB) model [32,33]. In a recent analytical study [34], the authors have demonstrated the emergence of Dirac Fermions owing to different symmetries of the system. The electronic and optical properties of non-hexagonal T-Graphene (TG) and SG nanoribbons are studied. It has been established that a mirror symmetry dependent multiple Dirac points emerge for armchair TGNRs [35]. In Refs. [36], authors have shown theoretically that doped TG quantum dots find its potential application in carbon monoxide gas sensor. Recently, Nath et al., by first principle calculation has shown that the bandgap of SGNRs are strongly dependent on the width and edge states of the NRs [37].

However, the inquiry and expectation of 2D allotropes of silicon are much constrained in contrast to 2D carbon allotropes because of complexities in the synthesis of Si-based 2D materials. Very few stable free-standing silicene allotropes were predicted such as MoS_2-type silicene [38], few honeycomb dumbbell silicene [39–41], tetragonal-silicene (TS) [42,43] similar to TG, tetra-silicene [44], 4-layered siliconeet [45] and monolayer silicon allotropes deposited on *c*-BN(111) [46]. Among the predicted silicene allotrope TS, siliconeet, and monolayer silicon allotropes deposited on *c*-BN(111) have Dirac cones. The TS structure predicted by Wu et al. [42], has a non-hexagonal symmetry and has two distinct Dirac points in the IBZ at the Fermi level. Owing to its buckling, TS has proximity towards sp^3 hybridization similar to silicene. Moreover, a bandgap opening is observed in TS on hydrogenation which can be modulated by biaxial strain, showing flexibility on electronic band structures [42,47]. The presence of two Dirac cones in IBZ, non-hexagonal symmetry, sp^3 hybridization makes TS an intriguing 2D material and henceforth requires extensive investigation.

Persuaded by these theoretical findings, we analyze the mechanical and electronic properties of the TS sheet and TS-nanoribbons (TSNR). In this work, we employ both the density functional theory (DFT) and the TB model to extract the electronic properties and behavior of the TS sheet as well as TSNRs. The paper is organized as follows. In section. 2, we present the DFT computational details employed in our work. In the 'Results and Discussions' section, we first discuss the structure of TS and compare it with the previous works. We have also analyzed the mechanical stability and elastic properties of the TS sheet. In the next part, we calculate the BS of TS sheet and employ the simple TB model to validate the existence of Dirac cones and investigate the stability and robustness in terms of TB parameters. Finally, we calculate the BS of the TSNRs of different edge and width using DFT and investigate the dependence of BS on TB parameters.

2. Methodology

The first-principle calculation is a reliable way to predict material properties, nonetheless, a simple tight-binding (TB) calculation also captures essential features. In this paper, both the TB and DFT of first-principle approaches have been employed. While DFT calculation is a computationally expensive process restricting calculation on smaller systems, TB calculation is inexpensive where a larger system can be dealt with it. The DFT calculations are carried out using the QUANTUM ESPRESSO (QE) package [48,49], based on an iterative solution of the Kohn-Sham equations of the DFT in a plane-wave basis set. We choose the technique with generalized gradient approximation (GGA) of Perdew-Burke-Ernzerhof (PBE) [50] exchange-correlation using Projected Augmented Wave (PAW) [51,52]. Throughout the calculation, we set the kinetic energy cutoff for charge density at 360 Ry. For calculation of the ground state properties, the Brillouin zone (BZ) is sampled using a uniform $16 \times 16 \times 1$ and $16 \times 1 \times 1$ automatic Monkhorst-Pack (MP) [53] special *k* grid points for the sheet and nanoribbons respectively. A denser $24 \times 24 \times 1$ and $24 \times 1 \times 1$ Brillouin zone sampling is used for performing density of states (DOS) and projected density of states (PDOS) calculation along with the Gaussian broadening of 0.01 Ry for the sheet and NRs respectively. A vacuum region of more than 15 Å is kept between the TS layers to avoid interaction between neighboring layers. The geometry of the sheet is optimized until the maximum Hellmann-Feynman forces in each atom are less than 0.001 eV/Å. The convergence for kinetic energy cutoff, *k*-grid points, were checked by calculating the total energy and formation energy of the TS sheet.

3. Results and Discussions

3.1. Structure

The atomic structure of TS is shown in Fig. 1a, which is similar to TG. The optimized unit cell, comprising of 8 atoms, exhibits a square symmetry with the lattice constant of $a = 7.6074$ Å. Two types of *Si-Si* bond length are $l_1 = 2.252$ Å and $l_2 = 2.304$ Å, where l_2 forms the four-membered silicon ring and l_1 connects those ring (Fig. 1b). The structure has a buckling of $\Delta Z \sim 0.496$ Å, which is similar to that of silicene (0.44 Å) [10]. The optimized parameters of TS are in accordance with reported in Refs. [42,47]. We have used periodic boundary condition with lattice translation vectors as $\overrightarrow{R_x} = a\hat{x}$ and $\overrightarrow{R_y} = a\hat{y}$ along X- and Y-direction respectively. As already reported in Ref. [42], TS structure is

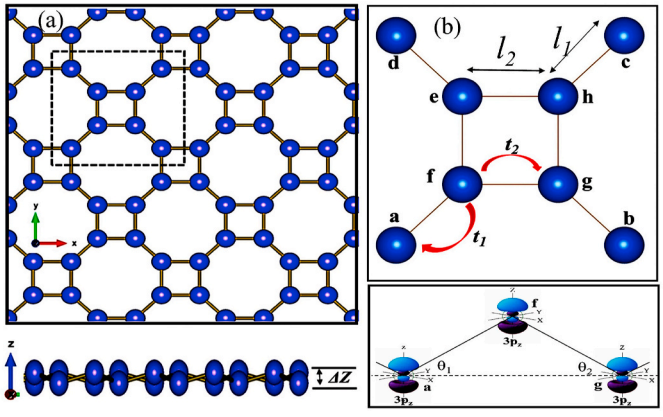

Fig. 1. (a) Optimized structure of TS with top and side views. The unit cell is marked with a box. (b) The unit cell with the hopping strenghts. (c) Buckling angle θ_1 and θ_2 w.r.t. *xy*-plane, only a portion of the unit cell with $3p_z$ orbitals are shown.

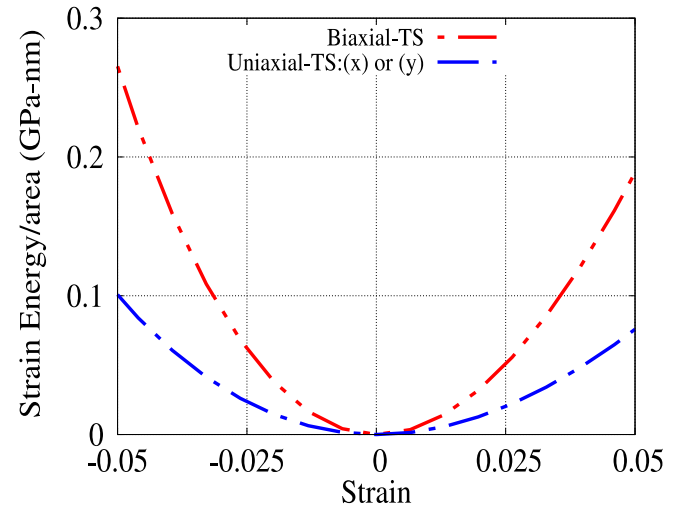

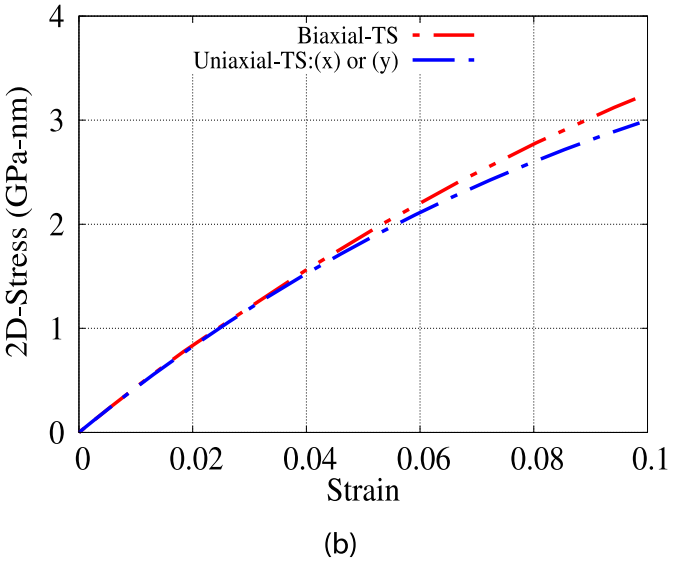

Fig. 2. (a) The strain energy/area of TS under uniaxial and equi-biaxial strain. (b) 2-D stress-strain curve.

stable at the ground state with no negative phonon modes. Also, the molecular dynamics study revealed that the atomic structure remains the same up to a temperature of 1000K. We have calculated the formation energy per atom of the TS sheet using $\Delta E_{TS} = (nE_{Si} - E_{TS})/\ n$, where $\Delta E_{TS}$is the formation energy, E_{Si} is the total energy of an isolated single *Si* atom, E_{TS} is the total energy of a unit cell of TS and $n(=8)$ is the number of TS atom per unit cell. The calculated value is 4.5837 eV/atom, slightly lower than the silicene (4.77 eV/atom), also confirming the stability of the structure.

3.2. Mechanical properties

In this section, we evaluate the mechanical properties and elastic constant of the T-Silicene sheet by calculating the change in energy due to in-plane strain. In standard Voigt notation, the strain energy per unit area of the two-dimensional structure can be expressed as [54].

$$u(\varepsilon) = \frac{1}{2}C_{11}\varepsilon_x^2 + \frac{1}{2}C_{22}\varepsilon_y^2 + C_{12}\varepsilon_x\varepsilon_y + 2C_{66}\varepsilon_{xy}^2 \quad (1)$$

where C_{11}, C_{22}, C_{12}, and C_{66} are components of the elastic modulus tensor, corresponding to the second partial derivative of strain energy

Table 1
Comparison of the in-plane stiffness E_a, E_b Poisson ratio ν and area modulus B of T-Silicene with silicene, Graphene, T-graphene, S-graphene and Penta-graphene. a and b denote the lattice vector direction of the unit cell of each 2D structure.

Structure	E_a (GPa-nm)	E_b (GPa-nm)	$\nu_a(\nu_b)$	B (GPa-nm)
T-Silicene [This work]	64.62	64.62	0.28	42.00
Silicene [55]	61.70	59.00	0.29 (0.33)	-
Graphene [56]	370.00	370.00	0.15	197.00
T-Graphene [56]	298.00	298.00	0.24	193.00
S-Graphene [37]	320.25	218.86	0.282 (0.193)	-
Penta-Graphene [54]	263.80	263.80	-0.068	-

with respect to strain. ε_x and ε_y are uniaxial in-plane strain along x and y directions respectively and ε_{xy} is the shearing strain. An absence of shearing strain leads to absence of the last term in equation (1). Since the TS structure is square symmetric, the value of C_{11} and C_{22} are equal, and we choose x direction for uniaxial strain. The elastic constants are evaluated by fitting the energy curves associated with uniaxial and equi-biaxial strains as shown in Fig. 2a. The obtained value of the elastic constants are $C_{11} = C_{22} = 70.295$ GPa-nm and $C_{12} = 19.977$ GPa-nm. The condition for the mechanical stability $C_{11}C_{22} - C_{12}^2 > 0$ is satisfied.

The in-plane stiffness, an alternative of Young modulus for 2D structures, along x or y direction is derived from the elastic constants by $E_a = E_b = (C_{11}^2 - C_{12}^2)/C_{11} = 64.618$ GPa-nm. The calculated Poisson ratio for the TS sheet is $\nu_{xy} = \nu_{yx} = C_{12}/C_{11} = 0.284$. These values are nearly equal to the values of silicene as reported in Ref. [55]. The alternative of the bulk modulus for 2D materials is the area modulus [57, 37], defined as $B = \frac{F/A}{\delta A/A}$ where F/A is the stress and $\delta A/A$ is the fractional change in the area (strain). The stress is calculated from the stress tensor obtained using QE. The structure is allowed to relax first, and then keeping the atomic position fixed, we have varied the area by elongating along x only (uniaxial) and both x and y direction (equi-biaxial) equally. The stress tensor is calculated using the self-consistent calculation for these uniaxial and biaxial strains. We have also plotted the stress-strain curve for the uniaxial and equi-biaxial conditions in Fig. 2b. Similar to other 2D materials, the TS sheet shows a non-linearity in its stress-strain curve. The area modulus from the linearly fitted stress-strain curves at small strain is $B \sim 42$ GPa. A comparative study of the elastic modulus (Table 1) suggests that TS is softer material compared to carbon-based 2D materials, while it is comparable to silicene. This lies in the fact that TS has a larger bond length with low buckling compared to carbon-based 2D materials.

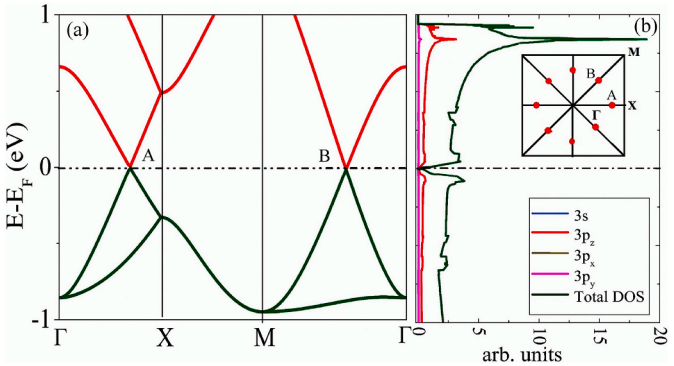

Fig. 3. (a)The electronic BS of TS and PDOS. The Fermi label is set to zero for convenience.(b) The DOS and PDOS of TS sheet. The path for the calculation of band structure in the BZ is shown in the inset. The dots represent the position of the Dirac points in the BZ.

3.3. Electronic properties of TS sheet

3.3.1. DFT results

In this subsection, we will investigate the electronic BS and density of states (DOS) of TS. The BS is calculated along the super-symmetry path $\Gamma(0,0,0)\rightarrow X(0.5,0,0)\rightarrow M(0.5,0.5,0)\rightarrow\Gamma(0,0,0)$ as shown in inset of Fig. 3b. The BS (Fig. 3a) shows that TS has two points in the IBZ where VB and CB meet in a single point at the Fermi level E_F (total eight points in the BZ). Thus, in the ground state, the TS behaves as a gapless insulator (semimetal) with two Dirac points. Around both the Dirac points, the conduction, and valance bands show linear dispersion, the point A with slope 2.94 eVÅ along X to Γ at $\vec{k} = \frac{2\pi}{a}(0.347, 0)$ and point B with slope 3.8 eVÅ along M to Γ at $\vec{k} = \frac{2\pi}{a}(0.441, 0.441)$. The Fermi velocity of TS is estimated by using,

$$v_F = \frac{1}{\hbar}\frac{dE}{dk}\Big|_{\vec{k}\rightarrow\vec{K}} \tag{2}$$

where $\vec{K}$ is the location of the Dirac point. Using this equation, we obtain the Fermi velocity to be $v_F \approx 0.45 \times 10^6$ m/s for point 'A' and $v_F \approx 0.58 \times 10^6$ m/s for point 'B'. This large value of v_F suggests the charge carriers for TS to be massless Dirac Fermions. Moreover, Dirac point 'B' lies slightly below E_F suggesting that TS is self-doped with electrons as charge carrier while Dirac point 'A' is intrinsic. Because the two points have different shapes and doping they will contribute differently to the electronic properties.

We have computed the projected density of states (PDOS) and DOS and is shown in Fig. 3b. The PDOS suggests that the contribution of the $3p_z$- orbitals is a maximum near E_F region. Consistently PDOS and DOS is zero at E_F.

Spin-orbit coupling (SOC) plays an important role in the electronic properties of Silicene [58]. Thus it can be expected that SOC will also play a crucial role in the electronic properties of the low-buckled TS. Hence, we have calculated the band structure of the TS sheet incorporating SOC using DFT and is shown in Fig. 4. We observe a spin-orbit bandgap of ~ 11.8 meV for the Dirac point 'A', while a gap of ~ 1.9 meV for the point 'B'. The spin-orbit gap at point 'A' and 'B' is nearly 7.5 times and 1.3 times, respectively, to that of the spin-orbit gap in Silicene ($E_g \sim 1.55$ meV) [17]. Moreover, the Dirac point 'A' lies slightly above the Fermi level indicating a self-doped character with the hole as carriers with the inclusion of SOC, which is otherwise intrinsic. On the other hand, the Dirac point 'B' becomes intrinsic with the SOC. This bandgap opening due to SOC and the alteration of the self-doping character of the Dirac cones of TS is of interest and, hence, requires intensive analysis. Since in this paper, we are not interested in the role of SOC in the electronic properties of the sheet or nanoribbons and hence are not carried out further. We emphasized only the band tuning by varying the TB parameters and structural modification (nanoribbons).

3.3.2. Tight-binding model

To validate the existence of Dirac points in the band structure and investigate the robustness and stability of the Dirac cones in the IBZ, we now avail of the nearest-neighbor (NN) tight-binding (TB) model considering the $3p_z$-orbital only, as these orbitals contribute near the Fermi level along with the formation of the Dirac cones.

A simple $3p_z$-electronic NN-TB model of TS requires two different NN hopping energy: t_1 and t_2 along the bond l_1 and l_2 respectively. Using the notation as in Fig. 1b, NN-TB Hamiltonian can be written as:

$$H_\pi^{nn} = \varepsilon\sum_i c_i^\dagger c_i + t_1(a^\dagger f + b^\dagger g + c^\dagger h + d^\dagger e + h.c.) + t_2(a^\dagger b + a^\dagger d + f^\dagger g + e^\dagger f + g^\dagger h + b^\dagger c + e^\dagger h + c^\dagger d + h.c.) \tag{3}$$

with ε as on-site energies of the atoms labelled $i \in \{a,b,c,d,e,f,g,h\}$.

To take care of the complicated buckling geometry the $3p_z$ orbitals can be decomposed into two components that are normal and parallel to the bond as in equation (4) and demonstrated in Fig. 5

$$\begin{aligned} |p_{zi}\rangle &= cos\,\theta_{ij}|p_{zi}^n\rangle + sin\,\theta_{ij}|p_{zi}^l\rangle \\ |p_{zj}\rangle &= cos\,\theta_{ij}|p_{zj}^n\rangle + sin\,\theta_{ij}|p_{zj}^l\rangle \end{aligned} \tag{4}$$

So, the hopping energy matrix element between the two neighboring atoms (i,j) is then given by

$$t_{ij} = \langle p_{zi}|c_i^\dagger c_j|p_{zj}\rangle = \langle p_{zi}^n|c_i^\dagger c_j|p_{zj}^n\rangle cos^2\,\theta_{ij} + \langle p_{zi}^l|c_i^\dagger c_j|p_{zj}^l\rangle sin^2\,\theta_{ij} = V_{pp\pi}^{ij} cos^2\,\theta_{ij} + V_{pp\sigma}^{ij} sin^2\,\theta_{ij} \tag{5}$$

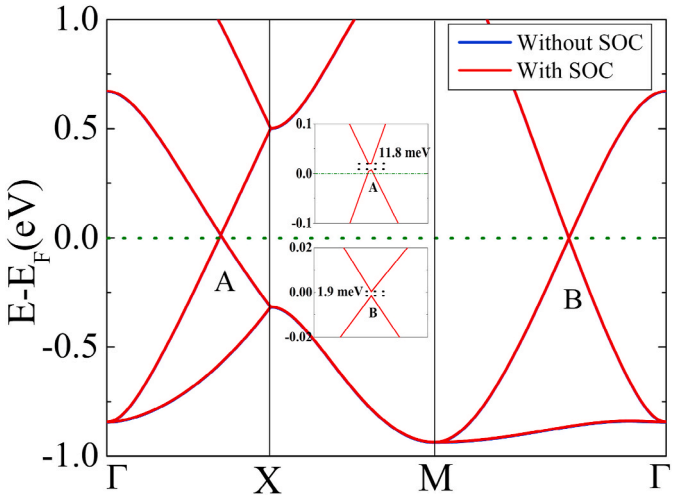

Fig. 4. Band diagram of TS sheet with and without spin-orbit Coupling. The insets show the zoom-in around the Dirac point A (top) and point B (bottom) with SOC.

where $V_{pp\pi}^{ij} = \langle p_{zi}^n|c_i^\dagger c_j|p_{zj}^n\rangle$, $V_{pp\sigma}^{ij} = \langle p_{zi}^l|c_i^\dagger c_j|p_{zj}^l\rangle$ are the two non-zero matrix elements.

Thus in our TB model the two different NN hopping energies t_1 and t_2

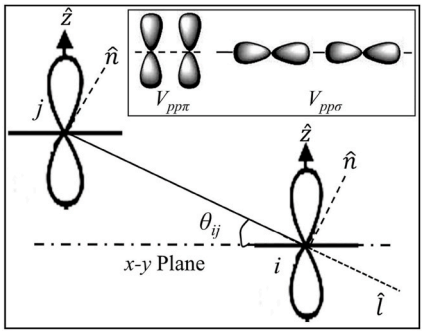

Fig. 5. Two neighboring p_z orbitals bonding making an angle θ_{ij} w.r.t. xy-plane and decomposition of the orbitals into normal and parallel components w.r.t bond direction $\vec{l}$. Pictorial representation of the non-vanishing components of hopping parameters are shown in the inset.

can be represented using $\langle ij\rangle = 1$ and 2 for bond l_1 and l_2 respectively, as

$$t_1 = V^1_{pp\pi}cos^2\theta_1 + V^1_{pp\sigma}sin^2\theta_1$$
$$t_2 = V^2_{pp\pi}cos^2\theta_2 + V^2_{pp\sigma}sin^2\theta_2 \quad (6)$$

where V's are the magnitudes of hopping parameters between NN $3p_z$orbitals, θ_1 and $\theta_2$are the buckling angles w.r.t. the xy-plane (Fig. 1c). From the stable structure data we have $sin\,\theta_1 = 0.2202$ and $sin\,\theta_2 = 0.2153$.

The Hamiltonian matrix is constructed in Bloch representation as

$$H^k_{ij} = \sum_{\vec{R}} e^{i\vec{k}\cdot\vec{R}} H_{ij}(R);\ H_{ij}(R) = \langle\phi_{\vec{o},i}|H|\phi_{\vec{R},j}\rangle \quad (7)$$

where H^k_{ij}'s are elements of 8×8 matrix, $|\phi_{\vec{R},j}\rangle$is the basis orbital of type j in cell $\vec{R}$, with $\vec{R} = a\hat{x} + a\hat{y}$ is lattice translational vector. The Hamiltonian matrix can be straight forwardly written using eqns. (3) and (7) as

$$H = \begin{pmatrix} \varepsilon & t_2\alpha & 0 & t_2\beta & 0 & t_1 & 0 & 0 \\ t_2\alpha^* & \varepsilon & t_2\beta & 0 & 0 & 0 & t_1 & 0 \\ 0 & t_2\beta^* & \varepsilon & t_2\alpha^* & 0 & 0 & 0 & t_1 \\ t_2\beta^* & 0 & t_2\alpha & \varepsilon & t_1 & 0 & 0 & 0 \\ 0 & 0 & 0 & t_1 & \varepsilon & t_2 & 0 & t_2 \\ t_1 & 0 & 0 & 0 & t_2 & \varepsilon & t_2 & 0 \\ 0 & t_1 & 0 & 0 & 0 & t_2 & \varepsilon & t_2 \\ 0 & 0 & t_1 & 0 & t_2 & 0 & t_2 & \varepsilon \end{pmatrix} \quad (8)$$

here $\alpha = e^{-ik_x a}$ and $\beta = e^{-ik_y a}$ with the wavevector $\vec{k} = k_x\hat{x} + k_y\hat{y}$. The diagonalization of this matrix readily gives the TB solution for energy dispersion relation.

3.3.2.1. Unification with DFT results. To check the consistency of our assumption for the NN-TB model we simulate the TB results and compare with DFT results for lowest energy bands near E_F. We have calculated the BS of TS corresponding to the Hamiltonian in equation (3) and is depicted in Fig. 6. For a better comparison of the band structure, we have shown the BS from both TB and DFT method in the same figure. For TB results we concentrate only on the two energy bands viz. upper VB (UVB) and lower CB (LCB) near the Fermi level. The system exhibits two Dirac cones similar to those obtained by DFT results. Though only p_z orbitals and simple NN-TB model cannot account the whole picture,

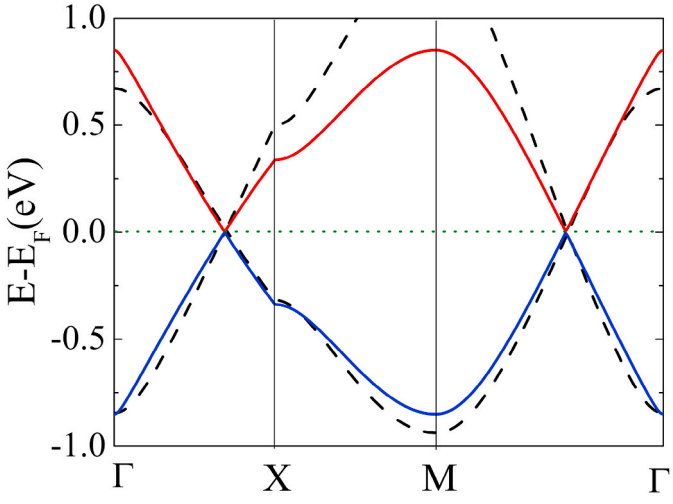

Fig. 6. Band structure of TS sheet corresponding to the TB Hamiltonian with NN hopping only. We set $t_1 = 0.85$eV, $t_2 = 0.9$ eV and $\varepsilon = 0.0$ eV to simulate the DFT result at Fermi level. The coloured line represents the TB results and black dotted lines the DFT results.

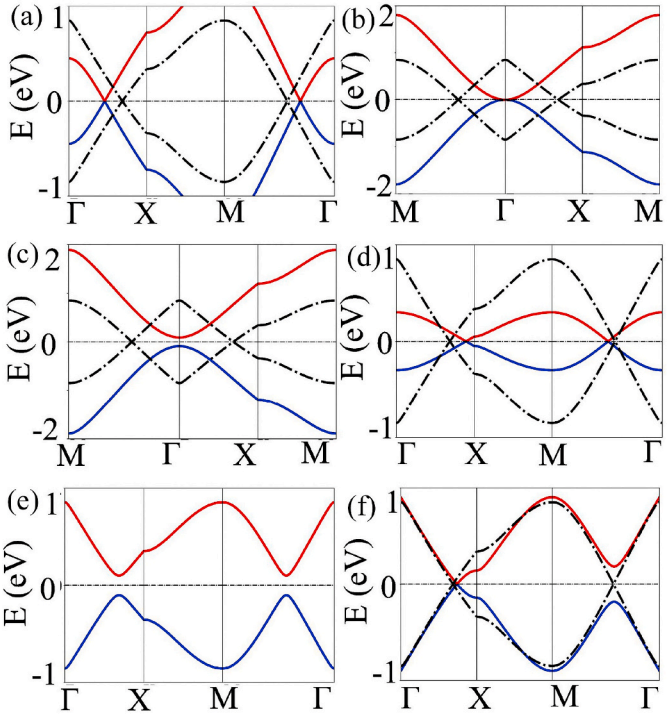

Fig. 7. (a) BS for $t_1/t_2 = 1.5$. The two Dirac points are shifted towards super-symmetric point Γ. (b) Merging of two Dirac points to a single flat region at Γ for $t_1/t_2 = 2.0$. Existence of a single Dirac point at the center of the Brillouin zone. (c) Bandgap opening for $t_1/t_2 > 2.0$. (d) Shifting of Dirac points A, B towards super-symmetric point X, M respectively for arbitrary $t_1/t_2 = 0.3$. (e) A bandgap opening for asymmetry in the on-site energy $\varepsilon = \pm 0.1$ eV and vice versa for alternate atoms with hopping parameter $t_1/t_2 = 0.85/0.9$. (f) Degeneracy of the point 'B' is removed with the asymmetry in the on-site energy, here we set $\varepsilon = \pm 0.3$ eV and vice versa for the alternate tetra-rings of Si-atoms. In the figure, solid blue (red) lines represents the UVB (LCB) for the aforementioned values of hopping energy and on-site energy, broken black lines are for $t_1/t_2 = 0.85/0.9 = 0.944$and $\varepsilon = 0.0$ as considered in Fig. 6 as a reference. (For interpretation of the references to colour in this figure legend, the reader is referred to the Web version of this article.)

Table 2
Tight binding hopping parameters of TS.

Parameters	$V^1_{pp\sigma}$	$V^2_{pp\sigma}$	$V^1_{pp\pi}$	$V^2_{pp\pi}$
Values in eV	4.47	4.42	−1.12	−1.16

taking the best fit of the BS using the NN-TB method with that obtained from the DFT near the Fermi level, we have calculated the optimized values of $t_1 = 0.85$ eV and $t_2 = 0.9$ eV. Further, we set the on-site energies of the TB model equal to zero $\varepsilon = 0.0$. Now, from the stable structure configuration, we have obtained $\theta_1 = sin^{-1}(0.2202)$ and $\theta_2 = sin^{-1}(0.2153)$ and using $t_1 = 0.85$ eV and $t_2 = 0.9$ eV in equation (6), we have calculated the four hopping paramters $V^1_{pp\sigma}$, $V^2_{pp\sigma}$, $V^1_{pp\pi}$, $V^2_{pp\pi}$ which is tabulated in Table 2. Two different sets of V correspond to two types of bonds in the TS structure. With these sets of values, the energy dispersion relation near E_F matches well with the DFT results particularly the position of Dirac points ($\vec{K} = \frac{2\pi}{a}(0.338, 0), \frac{2\pi}{a}(0.411, 0.411)$ for A, B point respectively) and the slope (3.0, 3.56 eVÅ for A, B point respectively towards Γ) of these points at Fermi energy. Even though different groups of t_1 and t_2 having same $t_1/t_2 \sim 0.944$ conserves the $\vec{K}$-positions of the Dirac points, the slope of bands near the Fermi level deviates from the DFT results. We have shown the results of two such groups in the Electronic Supplementary Item (ESI) Fig. 1. The symmetry of the TB

band spectra around the Fermi level is due to electron-hole symmetry. The values of $V_{pp\sigma}$ and $V_{pp\pi}$ matches well with that of silicene [58].

3.3.2.2. Robustness of the Dirac points. Now we investigate the robustness and stability of the individual Dirac cones of TS by tuning the hopping energy and on-site energy from their value obtained by fitting DFT parameters. We consider the cases when (i) $t_1/t_2 > 1.0$, (ii) $t_1/t_2 < 1.0$ and (iii) asymmetry in the on-site energy.

(i) With the increase in t_1/t_2 above unity, the BS remains gapless with the existence of both the Dirac points. However, both the Dirac point, 'A' and 'B' move in the direction towards Γ super-symmetric point to new $\vec{k}$ position at the same Fermi level. A typical band structure for arbitrary value of $t_1/t_2 = 1.5$ is shown in Fig. 7a. At $t_1/t_2 = 2.0$ the two Dirac points in the IBZ merge at Γ super-symmetric point and the energy dispersion becomes metallic in nature (Fig. 7b). The highest VB and lowest CB become flat and appear to meet at a small region, but without any linear dispersion in the energy relation. Upon further perturbation ($t_1/t_2 > 2.0$), there is a bandgap opening in the energy dispersion and both the Dirac points disappear (Fig. 7c). With further increase in t_1/t_2, the gap opening increases.

(ii) For $t_1/t_2 < 1.0$, the Dirac points 'A' and 'B' move toward super-symmetric point *X* and *M* respectively as shown in Fig. 7d. The Dirac points shift unequally towards supersymmetric points but they do not merge to a single Dirac point and both of them exist for any value of $t_1/t_2 < 1.0$. We have observed that for $t_1/t_2 \rightarrow 0$ the point 'A' meets to high-symmetric point *X* whereas the point 'B' stays at the middle point of the super-symmetric line *M* - Γ. At $t_1/t_2 = 0.0$ i.e no hopping of electrons between inter-four-member Si tetra-rings and/or infinite hopping probability in the intra-Si tetra-rings, an insulating behavior is observed. This is due to the breaking of the periodicity of the TS in either direction which may behave as a TS quantum dot. Based on these results, we obtain the criterion for the existence of two Dirac points in the IBZ as

$$0.0 < \frac{t_1}{t_2} < 2.0 \tag{9}$$

The change in hopping energy ratio corresponds to change in hopping matrix parameters ($V^{ij}_{pp\pi}$, $V^{ij}_{pp\sigma}$) and angle ($cos\,\theta_{ij}$, $sin\,\theta_{ij}$) of the buckled structure w.r.t. *xy*- plane.

It is to note that the slope of the bands near E_F can be achieved by tuning the Dirac cone with the modification of hopping parameters, which in turn modifies the carrier mobility significantly. To realize the feasibility of band tuning by the hopping parameters, we apply uniaxial and biaxial stress up to 5% using DFT (not shown). We have observed that the Dirac cones remain intact with shifting of the point position accordingly, depending upon elongation or compression. So, Dirac points in TS are rather robust under the application of strain i.e separation (overlap of orbitals) between the neighboring atoms. Similar behavior was also observed for graphene [59,60].

(iii) Now we consider the case when the on-site symmetry within the unit cell is broken, keeping hopping energy unchanged ($t_1 = 0.85eV$, $t_2 = 0.9eV$). For this, we consider two cases as,

(a) The on-site energy of alternate atoms have different values as

$$\begin{aligned} \varepsilon_1 &= \varepsilon_{i\in\{a,c,e,g\}} = +\delta \\ \varepsilon_2 &= \varepsilon_{i\in\{b,d,f,h\}} = -\delta \end{aligned} \tag{10}$$

Thus the atom with $+\delta$ on-site energy is connected with NN atoms with on-site potential $-\delta$ and vice-versa. We observe a bandgap opening is induced in the system even with the presence of small anisotropy in the on-site potential (Fig. 7e). This result is the consequence of the breaking of reflection symmetry, with time-reversal symmetry being intact in the system.

(b) The on-site energy of the atoms of alternate Si-tetra rings are different as

$$\begin{aligned} \varepsilon_3 &= \varepsilon_{i\in\{a,b,c,d\}} = +\delta \\ \varepsilon_4 &= \varepsilon_{i\in\{e,f,g,h\}} = -\delta \end{aligned} \tag{11}$$

Thus all the atom of a *Si* tetra-ring having on-site potential $+\delta$ is connected with four Si tetra-ring with all atoms in those rings having on-site energy $-\delta$. It is observed that a small anisotropy in this form lifts the degeneracy of Dirac cone 'B' while keeping the Dirac cone 'A' intact as shown in Fig. 7f. However, the Dirac point 'A' moves toward super-symmetric point *X*.

The stability and the robustness of the two Dirac cones of TS are quite different from another non-hexagonal graphene allotrope S-Graphene (SG), having two Dirac cones in the IBZ. The degeneracy of the individual Dirac cones as well as both the Dirac cones of SG can be removed by the conditions solely determined by the hopping parameters [32]. However as discussed, the degeneracy of the individual Dirac cones in TS cannot be lifted only by tuning the hopping parameters. This feature is quite interesting as the Dirac nature of the material remains inherent and is independent over a wide range of hopping parameters.

3.4. Structural model for TSNRs

One of the ways for bandgap tuning of 2D materials can be obtained by structural tailoring of the sheet as ribbons with different edge geometry and width. Nanoribbons with armchair edges (ATSNR) and zigzag edges (ZTSNR) of different width are cut along *x*- and *xy*-axis (45^0

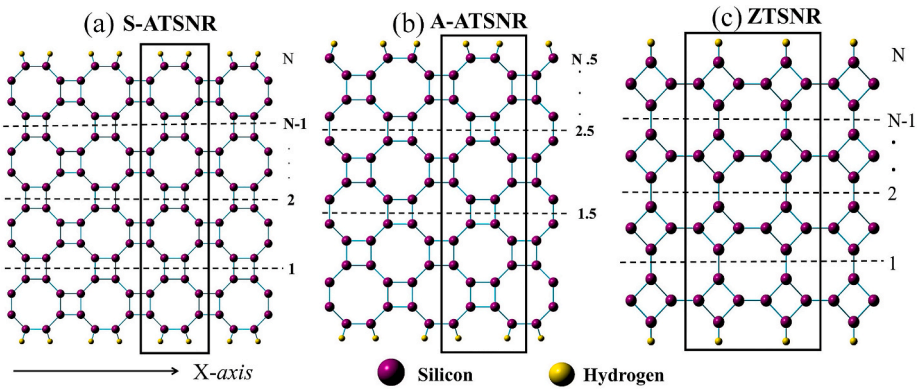

Fig. 8. Structure of (a) S-ATSNR (b) A-ATSNR (c) ZTSNR.

Table 3
Formation energy per atom E_f in eV/atom of the TSNRs. N is integer for S-ATSNR and ZTSNR, and half integer for A-ATSNR.

N	S-ATSNR	A-ATSNR	ZTSNR
1/1.5	3.7619	3.9726	3.6397
2/2.5	4.0898	4.1750	4.0489
3/3.5	4.2323	4.2765	4.1985
4/4.5	4.3102	4.3381	4.2860
5/5.5	4.3593	4.3785	4.3411

with the x axes) respectively from the relaxed sheet as shown in Fig. 8. The ATSNR with width N can be divided into two groups viz. integer (half-integer) based on the opposite edges are symmetric (asymmetric), where N denotes the primitive unit cell of the TS. The ZTNRs has a lattice constant of 10.7588 Å. The width of the ZTSNR denotes the number of two interconnected tetra-rings in each unit cell as shown in Fig. 8c. The dangling bonds are passivated with hydrogen and are further relaxed until the residual force on each atom of TSNRs is converged below 0.02 eV/Å. To avoid spurious interactions between the periodically repeated replicas of the ribbon, a vacuum region of 15 Å is set in the directions perpendicular to the ribbon axis. After optimizing, the $Si-Si$ bond length is 2.30–2.31 Å and 2.25–2.26 Å for Si-tetra-rings and between NN tetra-rings respectively. The $Si-H$ bond length is 1.50 Å.

We checked the stability of TSNRs by calculating the formation energy E_f per atom of the nanoribbons by using the equation,

$$E_f = \frac{\left(E^{tot}_{TSNR} - N_{Si}E_{Si} - N_H E_H\right)}{N_{Si} + N_H} \tag{12}$$

where E^{tot}_{TSNR}, E_{Si}, E_H are the total energy of the TSNRs, single Si atom, and a spin polarised hydrogen atom respectively. N_{Si} and N_H are the number of Si and H atom in the TSNR. The values of E_f for symmetric ATSNR (S-ATSNR), asymmetric ATSNR (A-ATSNR), and ZTSNR are tabulated in Table 3. A positive value of E_f suggests that TSNRs are stable and the values are comparable to the TS sheet (4.58 eV/atom). However, the stability of the narrowest NRs of each type is the least.

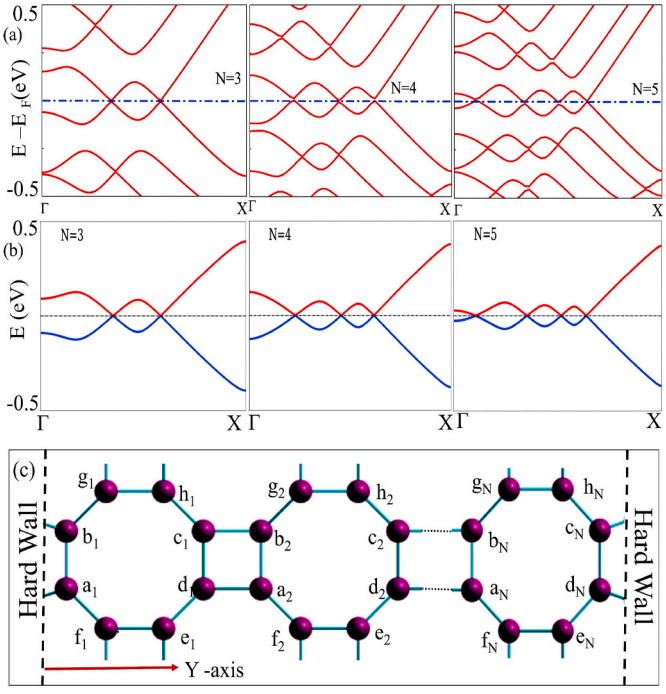

Fig. 9. (a) Band structure of S-ATSNR for width $N = 3$-5 calculated by DFT. E_F is set to zero. (b) BS of S-ATSNR from TB model for $N = 3$-5. (c) Unit cell for S-ATSNR showing the periodicity of the atoms used for TB calculation. For the TB BS calculation we have set $t_1 = 0.85$ eV and $t_2 = 0.9$ eV.

3.5. Electronic properties of TSNRs

Both the DFT and TB method are employed to construct and understand the BS of the nanoribbons. The BS is calculated along the path Γ to X of the BZ. A simple $3p_z$-orbital NN-TB model is taken to explain the electronic structure of the TSNRs. To validate this assumption, we also performed the PDOS calculation for the TSNRs (not shown), which suggests that only $3p_z$ orbitals contribute near the Fermi energy.

3.5.1. Symmetric ATSNR

The band structure of S-ATSNR for $N = 1$-5 is calculated using DFT. We have shown the band structure for N = 3-5 only in Fig. 9a. It is clear from the figure that multiple Dirac cones appear in the BS of A-ATSNR with the number of the Dirac cone depending on the width N of A-ATSNR.

We have also calculated the BS of the S-ATSNRs using the NN-TB model. The unit cell of S-ATSNR having width N is shown in Fig. 9c. The periodic boundary condition with lattice translation vectors as $\overrightarrow{R_x} = a\hat{x}$ is along x-direction only with $a = 7.6074$ Å. Hard walls are imposed at the edge boundary in y-direction, i.e. amplitudes of the basis wavefunctions will be zero beyond the hard wall. Due to this restriction in y-direction for the NRs, there will be some modification in on-site energy and hopping energy near the edge, though the difference is expected to be small. Here we have argued that since there is nearly no change in bond length as obtained from DFT calculations, we neglect this difference and considered two types of NN hopping energy t_1 and t_2 as defined earlier with zero electronic transfer through the hard wall. We also set all the on-site energies ε as zero. TB Hamiltonian matrix with the help of equation (7) can be written as $N \times N$ tridiagonal matrix as

$$H_N = \begin{pmatrix} H_b & H_i & 0 & \cdots & 0 \\ H_i^\dagger & H_b & H_i & \cdots & 0 \\ 0 & H_i^\dagger & H_b & \ddots & 0 \\ \vdots & \vdots & \ddots & \ddots & H_i \\ 0 & 0 & \cdots & H_i^\dagger & H_b \end{pmatrix} \tag{13}$$

where all the elements of the matrix is itself a 8×8matrix. The matrix H_b has the form of

$$H_b = \begin{pmatrix} 0 & t_2 & 0 & 0 & 0 & t_1 & 0 & 0 \\ t_2 & 0 & 0 & 0 & 0 & 0 & t_1 & 0 \\ 0 & 0 & 0 & t_2 & 0 & 0 & 0 & t_1 \\ 0 & 0 & t_2 & 0 & t_1 & 0 & 0 & 0 \\ 0 & 0 & 0 & t_1 & 0 & t_2 & 0 & t_2\alpha^* \\ t_1 & 0 & 0 & 0 & t_2 & 0 & t_2\alpha^* & 0 \\ 0 & t_1 & 0 & 0 & 0 & t_2\alpha & 0 & t_2 \\ 0 & 0 & t_1 & 0 & t_2\alpha & 0 & t_2 & 0 \end{pmatrix} \tag{14}$$

H_i is very sparse matrix with only two non-zero elements, $\langle c_{N-1}\left|\hat{H}\right|b_N\rangle = \langle d_{N-1}\left|\hat{H}\right|a_N\rangle = t_2$. We have diagonalized equation (13) numerically and focus only on the two energy bands (UVB and LCB) near the Fermi level. Multiple Dirac points appear at the Fermi level, with the number increasing with the increase in the width of the NRs. The number of Dirac cones exhibit three-member family behavior. For instance, $N = 1,2$ number of Dirac cones is N; for $N = 3, 4, 5$ number of Dirac cones are $N-1$; for $N = 6, 7, 8$ number of Dirac cones are $N-2$; for $N = 9, 10, 11$ number of Dirac cones are $N-3$ and so on. The typical band structure for $N = 3$-5 S-ATSNR using TB is depicted in Fig. 9b. The BS for larger N (=6-10) is shown in ESI Fig. 2, which shows the number of Dirac cones for each width of S-ATSNRs.

Now we examine the stability of these Dirac cones by varying the

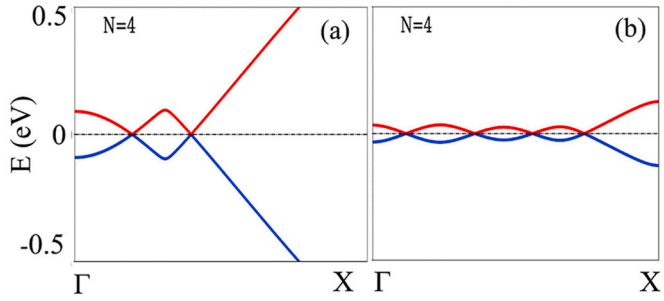

Fig. 10. (a) Decrease in the number of Dirac points, we set $t_1/\ t_2\ =\ 1.5$. (b) Increase in the number of Dirac points, we set $t_1/t_2\ =\ 0.5$.

hopping parameters. We have solved numerically equation (13) for different values of t_1/t_2 and results for S-ATSNR of width $N\ =\ 4$ are presented in Fig. 10. We observe that with the increase in $t_1/\ t_2$ (>1) number of Dirac points decreases one by one and ultimately at $t_1/\ t_2\ =$ 2.0 all the Dirac points disappear and band opening occurs. The NR becomes a semiconductor. This feature is quite similar to that of the TS sheet as discussed earlier. Here we have shown the BS for $N\ =\ 4$ at arbitrary value $t_1/t_2\ =\ 1.5$, which shows existence of only two Dirac cones (Fig. 10a). But, with the decrease in $t_1/t_2(<1)$, the number of Dirac points increases one by one and becomes equal to the width N of the NRs, though the band flattening occurs. Finally, the two bands are flattened to a line and meet the Fermi level at $t_1/t_2\rightarrow 0$. This result corresponds to a breaking of periodicity along the $x-$ axis, transforming the NR to a quantum dot. In Fig. 10b, we show the BS for $N=4$ exhibiting N Dirac cones for $t_1/t_2\ =\ 0.5$.

For S-ATSNR, the slope of the multiple Dirac points increases along Γ to X. For $N=4$, slopes of the Dirac points along Γ to X have values 1.8 eV, 2.18 eV and 2.63 eV. The corresponding Fermi velocity calculated using equation (2) are $v_F \approx 0.27\times 10^6$ m/s, 0.33×10^6 m/s, 0.4×10^6 m/s respectively along Γ to X. Thus, the velocity of Dirac Fermions increases along the super-symmetric line from Γ to X. In Fig. 11, we have plotted the Fermi velocity of the Dirac cone with a maximum magnitude of the S-ATSNRs (N = 3-9) calculated from the TB method. Fermi velocity obtained by DFT for $N=3$-5 is shown for comparison, which suggests TB and DFT predict the nearly same Fermi velocity. The values of the v_F are a little smaller than those obtained for the sheet. With the increase in width of the S-ATSNR, the Fermi velocity of the Dirac Fermions also increases gradually. It may be expected that at large N, the Fermi velocity of the S-ATSNR will match that of the sheet.

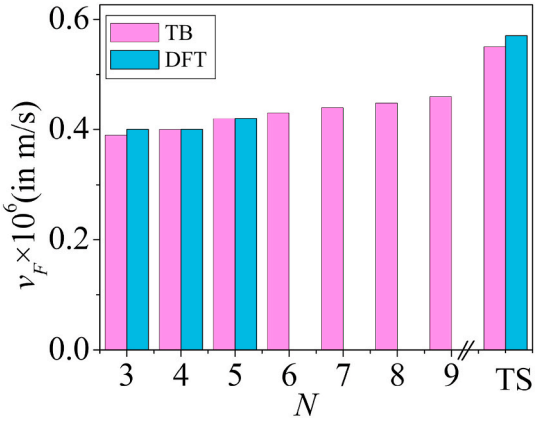

Fig. 11. Fermi velocity (v_F) of the Dirac cone with maximum value with width N of S-ATSNR calculated from TB. The DFT results for N = 3-5 are shown for comparison. The $v_F$for sheet is also shown.

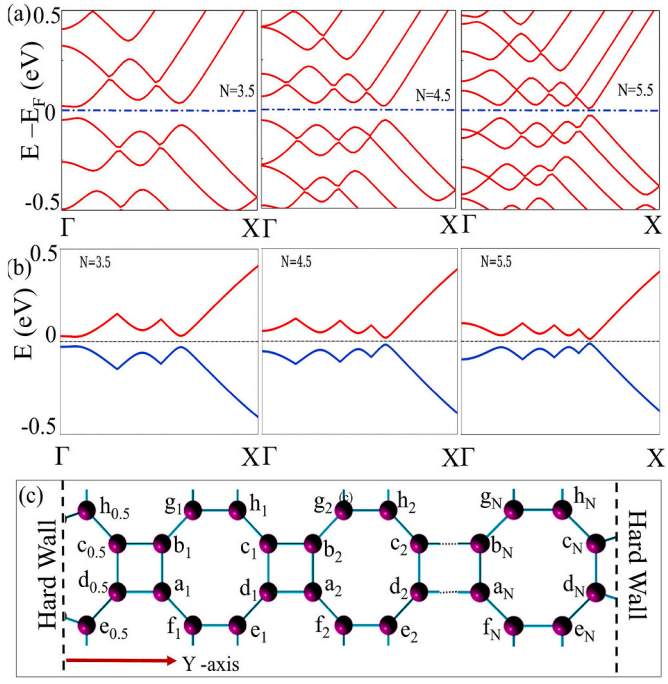

Fig. 12. (a) and (b) BS of A-ATSNR with N = 4.5–6.5 calculated by DFT and TB method respectively. We set t_1 = 0.85 eV, t_2 = 0.9 eV and ε = 0.0 eV in the TB calculation. (c) Unit cell of A-ATSNR. In DFT band structure E_F is set to zero for convenience.

3.5.2. *Asymmetric ATSNR*

The DFT results for BS of the A-ATSNR for N = 3.5, 4.5, and 5.5 are shown in Fig. 12a. A direct gap opening is observed for all N except $N=$ 1.5, where an indirect bandgap E_g is observed. The exception for $N=1.5$ arises due to the strong confinement effect and interaction between the edge states. Next, we numerically calculate the BS in the NN-TB framework. The unit cell of A-ATSNR having width $N\frac{1}{2}$ is shown in Fig. 12c. Similar to S-ATSNR, the periodic boundary condition with lattice translation vectors as $\overrightarrow{R_x} = a\hat{x}$ is along x-direction only with $a=$ 7.6074 and hard wall in y-direction. TB Hamiltonian matrix with the help of equation (7) can be written as $\frac{2N+1}{2}\times\frac{2N+1}{2}$ matrix as

$$H_{\frac{2N+1}{2}} = \left(\begin{array}{c|ccc} H_f & H_d & 0 & \cdots & 0 \\ \hline H_d^\dagger & & & & \\ 0 & & & H_N & \\ \vdots & & & & \\ 0 & & & & \end{array}\right) \tag{15}$$

where H_f is a $4\times$ 4matrix has the form of

$$H_f = \begin{pmatrix} 0 & t_2 & 0 & t_1 \\ t_2 & 0 & t_1 & 0 \\ 0 & t_1 & 0 & t_2\alpha^* \\ t_1 & 0 & t_2\alpha & 0 \end{pmatrix} \tag{16}$$

Table 4
Bandgap E_g in eV of A-ATSNR for different width obtained by DFT and TB.

NR width	DFT	TB
1.5	0.293	0.231
2.5	0.173	0.120
3.5	0.057	0.051
4.5	0.071	0.037
5.5	0.036	0.024
6.5	0.028	0.016

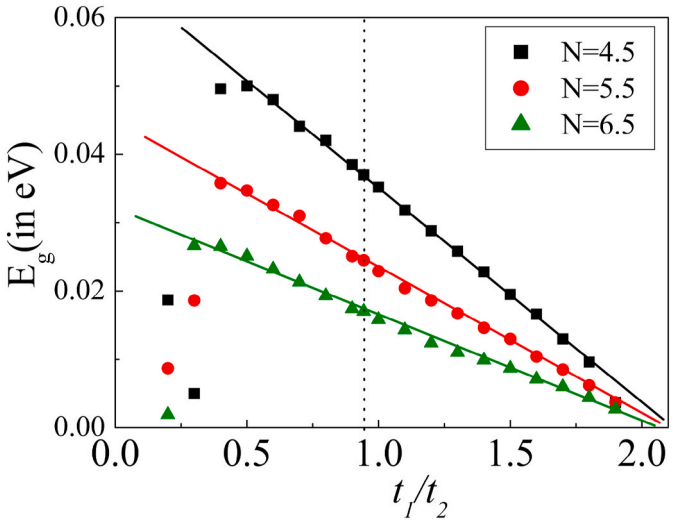

Fig. 13. Variation of bandgaps E_g with t_1/t_2 for $N = 4.5$, 5.5, and 6.5; straight lines are fitted in the linear region. The vertical dotted line represents the value optimized value of $t_1/t_2 = 0.944$.

and H_d is a 4×8 matrix with only two non-zero elements $\langle c_{0.5}\left|\widehat{H}\right|b_1\rangle = \langle d_{0.5}\left|\widehat{H}\right|a_1\rangle = t_2$ and all the zeros in first row are 4×8 matrix and zeros in the first column are 8×4 matrix. We have presented the typical values of the bandgap calculated by both DFT and TB results in Table 4.

Both the DFT and TB calculations predict a bandgap opening which decreases with the width of the A-ATSNR. Though the values differ, the qualitative feature is similar in both methods. This discrepancy may arise since we take only a simple NN-TB model to extract the physics of the system. A higher-order term in TB may effectively match the results. The opening of the bandgap for A-ATSNR is due to the broken reflection symmetry which enters into equation (15) through the H_f block. In Fig. 12b, we have shown the BS using TB method for $N = 3.5$–5.5.

The bandgap in A-ATSNRs is small and decreases gradually for width $N \geq 3.5$. The signature of these semiconducting behavior in nanoribbons may emerge due to the interaction between the exotic edge states. For $N \geq 3.5$ the edge states interact very weakly, which may result in small and nearly constant E_g. For small $N \leq 2.5$ larger bandgap originates from the quantum confinement along with the contribution from the highly interacting edge states.

We now evaluate the bandgap E_g as a function of hopping parameters t_1/t_2 for $N = 4.5$, 5.5, and 6.5 and is depicted in Fig. 13. For all the NRs a

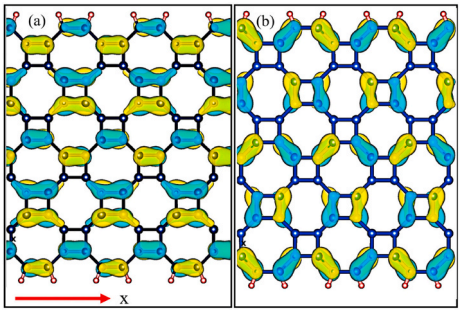

Fig. 14. The charge density of (a) HO and (b) LU band distribution of A-ATSNR with $N = 3.5$.

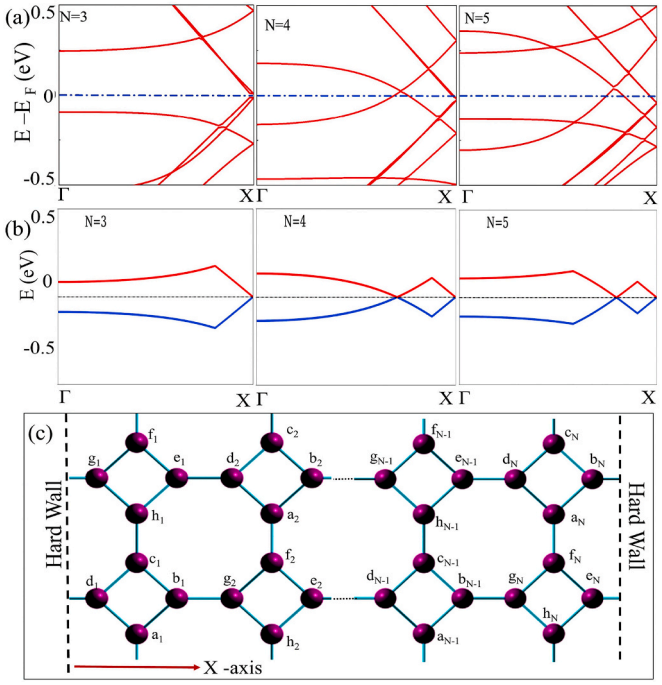

Fig. 15. (a) and (b) BS of ZTSNR with $N = 3$-5 obtained from DFT ($E_F = 0$ is set for convenience) and TB respectively. As previous, we have set $t_1 = 0.85$ eV, $t_2 = 0.9$ eV and $\varepsilon = 0.0$ eV (c) Unit cell for ZTSNR.

similar trend in bandgap variation is observed. For the NRs under consideration, maximum of E_g occurs when $t_1/t_2 \sim 0.4$. The bandgap then decreases linearly with t_1/t_2 and finally at $t_1/t_2 \approx 1.95$, $E_g \to 0$. The decrease in bandgaps E_g in the range $0.4 < t_1/t_2 < 2.0$ are observed to follow an equation

$$E_g \approx -N^{-2.22}\frac{t_1}{t_2} + N^{-1.82} \tag{17}$$

With the increase in t_1/t_2, the probability of hopping of an electron between inter Si-tetra ring atoms increases relative to the hopping between *Si*-atoms in the tetra rings. Or in other words, the increase in t_1/t_2, increases the overlap of the orbitals among the inter tetra-ring Si atoms (along l_1) relative to the intra-tetra-ring Si atoms (along l_2). This in turn decreases the bandgap. At a small value of t_1/t_2, the electron confinement leads to a large bandgap. With the increase of t_1/t_2, this electron confinement behavior reduces, resulting in a decrease in the bandgap energy. Thus, we can tune the bandgap of the A-ATSNR solely by the hopping parameters and modify the semiconducting A-ATSNR to metallic A-ATSNR. However, this kind of modification is again difficult to implement as the hopping parameter t_1 has to be increased by 100% or decrease t_2 by 50%. However, the tuning of the hopping parameters up to a certain limit can be achieved by strain or under the influence of external magnetic flux [61].

To understand the origin of band-gaps in A-ATSNRs, we have plotted the charge densities for the highest occupied (HO) and lowest unoccupied (LU) bands in Fig. 14 for arbitrary $N = 3.5$. It is evident from the figure that the HO bands are contributed by the $Si - Si$ bond of the tetra-rings along with the periodicity of the lattice i.e. l_2 bonds along the x axis. The LU band is contributed by the alternate l_1 and l_2 bonds perpendicular to the x axis.

3.5.3. ZTSNR

Fig. 15a depicts the BS for ZTSNR for $N = 3$-5 as obtained by DFT. The BS for $N = 1$ and 2 are also calculated (not shown). However, the structure of ZTSNR for $N = 1$ does not reflect the periodicity of the TS

sheet as can be observed in Fig. 15c. A very small bandgap $E_g \sim 0.02$ eV exists for $N = 2,3$ at the super-symmetric point X. With an increase of width $N \geq 4$, the system behaves as a degenerate semiconductor with two Dirac cones with a very small gap ~ 0.003 eV- one just below E_F and other just above E_F. The Dirac cone just below E_F appears at the super-symmetric point X. The DOS plot (not shown) also shows a zero density of states at the E_F.

We now employ the simple NN-TB Hamiltonian with π-orbitals only to extract the physics and behavior of these systems. The TB Hamiltonian matrix can be written using equation (7) as $N \times N$ as

$$H_N = \begin{pmatrix} H_1 & H_z & 0 & 0 & \cdots & \cdots & 0 \\ H_z^\dagger & H_2 & H_z & 0 & \cdots & \cdots & 0 \\ 0 & H_z^\dagger & H_1 & H_z & 0 & \cdots & 0 \\ \vdots & 0 & H_z^\dagger & H_2 & \ddots & \vdots & \vdots \\ \vdots & \vdots & \vdots & \ddots & \ddots & H_z & 0 \\ 0 & 0 & 0 & \cdots & H_z^\dagger & H_1 & H_z \\ 0 & 0 & 0 & \cdots & 0 & H_z^\dagger & H_2 \end{pmatrix} \tag{18}$$

Every element of the matrix is itself an 8×8 matrix, with

$$H_1 = \begin{pmatrix} 0 & t_2 & 0 & t_2 & 0 & t_1\alpha^* & 0 & 0 \\ t_2 & 0 & t_2 & 0 & 0 & 0 & 0 & 0 \\ 0 & t_2 & 0 & t_2 & 0 & 0 & 0 & t_1 \\ t_2 & 0 & t_2 & 0 & 0 & 0 & 0 & 0 \\ 0 & 0 & 0 & 0 & 0 & t_2 & 0 & t_2 \\ t_1\alpha & 0 & 0 & 0 & t_2 & 0 & t_2 & 0 \\ 0 & 0 & 0 & 0 & 0 & t_2 & 0 & t_2 \\ 0 & 0 & t_1 & 0 & t_2 & 0 & t_2 & 0 \end{pmatrix} \tag{19}$$

and

$$H_2 = \begin{pmatrix} 0 & t_2 & 0 & t_2 & 0 & t_1 & 0 & 0 \\ t_2 & 0 & t_2 & 0 & 0 & 0 & 0 & 0 \\ 0 & t_2 & 0 & t_2 & 0 & 0 & 0 & t_1\alpha \\ t_2 & 0 & t_2 & 0 & 0 & 0 & 0 & 0 \\ 0 & 0 & 0 & 0 & 0 & t_2 & 0 & t_2 \\ t_1 & 0 & 0 & 0 & t_2 & 0 & t_2 & 0 \\ 0 & 0 & 0 & 0 & 0 & t_2 & 0 & t_2 \\ 0 & 0 & t_1\alpha^* & 0 & t_2 & 0 & t_2 & 0 \end{pmatrix} \tag{20}$$

$H_z$is a very sparse matrix with only non-zero elements are $\langle b_{N-1}\left|\widehat{H}\right|g_N\rangle = \langle e_{N-1}\left|\widehat{H}\right|d_N\rangle = t_1$.

For comparison, we have reproduced TB results for N = 3-5 in Fig. 15b respectively. The number of Dirac points increases with the width of the NRs. Contrary to DFT results, the Dirac cones obtained by the NN-TB method appears at the Fermi level. Linearity in the energy dispersion towards 'X' super-symmetric point is observed. With the increase in the t_1/t_2 ratio, the number of Dirac points decreases, with the band becomes broadened gradually, and finally one Dirac point at super-symmetric point 'X' exists only at larger values of $t_1/\ t_2$ ($\sim$2). With the decrease of t_1/t_2, all Dirac points start shifting towards super-symmetric point 'X' with a continuous band flattening. In Fig. 16a and b we have shown the band structure for $N = 4$ and $t_1/t_2 = 1.5$ and 0.5 respectively.

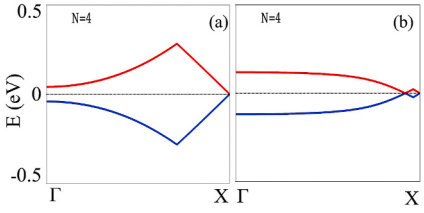

Fig. 16. (a) Decrease in the number of Dirac points, for an arbitrary value of $t_1/t_2 = 1.5$. (b) Shifting of the Dirac points for $t_1/t_2 = 0.5$. Here width $N = 4$.

Our theoretical study of the band tuning will motivate the scientific community for further and detailed research regarding its synthesis, application, and exploration of other properties. Whenever the experimental preparation of 2D TS sheets and TS nanoribbons are concerned, it is well known that any form of silicene whether hexagonal or tetragonal cannot be made by exfoliation as done in the case of graphene [62]. It turns out that Ag (111) surface is the most commonly used substrates for silicene due to the efficient controlled interaction between silicene and Ag having similar lattice constants. Apart from mechanical support, the substrate offers the opening of the bandgap without degrading the essential electronic properties of silicene. It is the essential van der Waals (vdW) interaction prevailing between silicene and substrate responsible for the sublattices' symmetry breaking leading to the opening of the bandgap. With the help of an appropriate catalyst, it might be possible to synthesize stable tetragonal silicene (T-silicene) on Ag/Au/Ir/ZrB_2/ZrC or other important 2D substrates at some critical temperature and pressure. Besides, various 2D substrates for T-silicene can lead to heterostructures having enough potential to be applicable for tunable and tiny electronic devices. The intriguing tunable characteristic features (direct and indirect) of the bandgap of hydrogenated 2D tetragonal silicenes under biaxial strain may indicate some futuristic applications in spintronic devices [47]. The interplay of SOC may open up new directions in the topological aspect of this material [17,58]. If T-silicene is synthesized, then nanolithography technology can be used to design various TS nanoribbons with diverse edge states and symmetry. The interplay of various Dirac cones in TS nanoribbons may lead to some exotic potential applications in spintronics, FETs, and sensors in the near future.

4. Conclusion

In this work, we systematically explore the mechanical and electronic properties of the stable non-hexagonal silicon allotrope T-silicene sheets and nanoribbons. We employ both first-principle calculation as well as the NN-TB model to explore the intriguing physics involved in the band structure of these systems. The TS sheet is mechanically stable with the elastic constants being comparable with that of silicene. The band structure of the TS sheet exhibits two Dirac cones at E_F in the IBZ suggesting a semi-metallic behavior with a negligible effect of SOC on the band structure. Fermi velocity calculation indicates that the charge carriers behave as massless Dirac fermions. The results obtained by the TB method conform to the DFT results. The TB hopping parameter values for the TS sheet are identical to that of silicene. The Dirac points of the sheet are robust and stable for a wide range of hopping energy ratios, i.e. $0.0 < t_1/t_2 < 2.0$. A small anisotropy in the on-site energy between alternate atoms lifts the degeneracy of the Dirac cones. The degeneracy of the Dirac cone 'B' (on $\Gamma - M$ symmetry path) is only removed with the introduction of asymmetry in the on-site energy of the alternate Si tetra-rings. The NRs cut from the TS sheet are stable and their electronic properties strongly depend on the width and the edge. The band structure of S-ATSNR shows multiple Dirac points in the IBZ, depending on the width of the NRs. The number of Dirac cones of S-ATSNR depends on the hopping parameters and is equal to the width N of the NRs for small TB hopping ratio ($t_1/t_2 < 1.0$). The A-ATSNR shows a semiconducting nature, with a bandgap decreasing gradually with the increase of width as well as the ratio t_1/t_2. DFT results predict that ZTSNR is a degenerate semiconductor with the presence of Dirac cones just below and above the Fermi level. The signature of the metal/semiconductor behavior of the NRs may be due to their crucial edge states. While symmetric edge states of S-ATSNR and ZTSNR give rise to Dirac features in the nanoribbons, asymmetric edge states in A-ATSNR show a gap opening in the band structure. The tuning of the band structure of the TS by tailoring into NRs and/or modulating the hopping parameters may motivate the experimentalist for its synthesis and future application in nano-electronics.

Author contribution statement

NSM: Simulations, Formal Analysis, Writing original draft **SN**: Conceptualization, Simulations, Formal Analysis, Writing **original** draft **DJ**: Formal Analysis, Discussions, Finalizing manuscript **NKG**: Formal Analysis, Finalizing manuscript, Discussions

Declaration of competing interest

The authors declare that they have no known competing financial interests or personal relationships that could have appeared to influence the work reported in this paper.

Acknowledgment

NSM and SN thank Arka Bandyopadhyay, University of Calcutta for stimulating discussions. One of the authors (NSM) acknowledges the computational suggestion of the Physics Teachers VU group.

Appendix A. Supplementary data

Supplementary data to this article can be found online at https://doi.org/10.1016/j.jpcs.2020.109801.

References

[1] K.S. Novoselov, A.K. Geim, S.V. Morozov, D. Jiang, Y. Zhang, S.V. Dubonos, I. V. Grigorieva, A.A. Firsov, Science 306 (2004) 666.
[2] F. Bonaccorso, Z. Sun, T. Hasan, A.C. Ferrar, Nat. Photon. 4 (2010) 611.
[3] F. Schweirz, Nat. Nanotechnol. 5 (2010) 487.
[4] M.J. Allen, V.C. Tung, R.B. Kaner, Chem. Rev. 110 (1) (2010) 132.
[5] A.A. Baladin, Nat. Mater. 10 (2011) 569.
[6] A.K. Geim, K.S. Novoselov, Nat. Mater. 6 (2007) 183.
[7] J. Haskins, A. Kınacı, C. Sevik, H. Sevinçli, G. Cuniberti, T. Çağın, ACS Nano 5 (2011) 3779.
[8] K.S. Novoselov, A.K. Geim, S.V. Morozov, D. Jiang, M.I. Katsnelson, I. V. Grigorieva, S.V. Dubonos, A.A. Firsov, Nature (London) 438 (2005) 197.
[9] C. Lee, X.D. Wei, J.W. Kysar, J. Hone, Science 321 (2008) 385.
[10] S. Cahangirov, M. Topsakal, E. Aktürk, H. Şahin, S. Ciraci, Phys. Rev. Lett. 102 (2009), 236804.
[11] B. Lalmi, H. Oughaddou, H. Enriquez, A. Kara, S. Vizzini, B. Ealet, B. Aufray, Appl. Phys. Lett. 97 (2010), 223109.
[12] S. Balendhran, S. Walia, H. Nili, S. Sriram, M. Bhaskaran, Small 11 (2015) 640.
[13] S. Chowdhury, D. Jana, Rep. Prog. Phys. 79 (2016), 126501.
[14] N. Dhar, D. Jana, J. Phys. Chem. Solid. 115 (2018) 332.
[15] P. Vogt, P.D. Padova, C. Quaresima, J. Avila, E. Frantzeskakis, M.C. Asensio, A. Resta, B. Ealet, G.L. Lay, Phys. Rev. Lett. 108 (2012), 155501.
[16] L. Meng, Y. Wang, L. Zhang, S. Du, R. Wu, L. Li, Y. Zhang, G. Li, H. Zhou, W. A. Hofer, H.J. Gao, Nano Lett. 13 (2013) 685.
[17] C.C. Liu, W.X. Feng, Y.G. Yao, Phys. Rev. Lett. 107 (2011), 076802.
[18] A. Dyrdal, J. Barnas, Phys. Status Solidi (RRL) 6 (2012) 340.
[19] Y.W. Son, L.M. Cohen, S.G. Louie, Phys. Rev. Lett. 97 (2006), 216803.
[20] M.Y. Han, B. Ozyilmaz, Y. Zhange, P. Kim, Phys. Rev. Lett. 98 (2007), 206805.
[21] Z. Chem, Y.M. Lim, M.J. Rooks, P. Avouris, Physica E 40 (2007) 228.
[22] C. Lian, Z. Yang, J. Ni, Physica B 561–2 (2012) 77.
[23] Y. Ding, J. Ni, Appl. Phys. Lett. 95 (2009), 083115.
[24] S.M. Aghaei, I. Calizo, J. Appl. Phys. 118 (2015), 104304.
[25] J. Kang, F. Wu, J. Li, Appl. Phys. Lett. 100 (2012), 233122.
[26] A. Majumdar, S. Chowdury, P. Nath, D. Jana, RSC Adv. 4 (2014) 32221.
[27] S.M. Aghaei, M.M. Monshi, I. Calizo, RSC Adv. 6 (2016) 94417.
[28] A.N. Enyashin, A.L. Ivanovskii, Phys. Status Solidi B 248 (2011) 1879.
[29] D. Malko, C. Neiss, F. Vines, A. Gorling, Phys. Rev. Lett. 108 (2012), 086804.
[30] Y. Liu, G. Wang, Q. Huang, L. Guo, X. Chen, Phys. Rev. Lett. 108 (2012), 225505.
[31] L.C. Xu, R.Z. Wang, M.S. Miao, X.L. Wei, Y.P. Chen, H. Yan, W.M. Lau, L.M. Liu, Y. M. Ma, Nanoscale 6 (2014) 1113.
[32] A. Bandyopadhyay, S. Datta, D. Jana, S. Nath, M.M. Uddin, Sci. Rep. 10 (2020) 2502.
[33] X. Qin, Y. Liu, G. Yang, D. Zhao, Phys. Chem. Chem. Phys. 22 (2020) 6619.
[34] A. Bandyopadhyay, D. Jana, Universal J. Mat. Science 8 (2) (2020) 32.
[35] C.J. Dai, X.H. Yan, Y. Xiao, Y.D. Guo, Eur. Phys. Lett. 107 (2014), 37004.
[36] A. Bandyopadhyay, S. Paria, D. Jana, J. Phys. Chem. Solid. 123 (2018) 172.
[37] S. Nath, A. Bandyopadhyay, S. Datta, D. Jana, M.M. Uddin, Physica E 120 (2020), 114087.
[38] F. Gimbert, C.C. Lee, R. Friedlein, A. Fleurence, Y.Y. Takamura, T. Ozaki, Phys. Rev. B 90 (2014), 165423.
[39] S. Cahangirov, V.O. Özcelik, A. Rubio, S. Ciraci, Phys. Rev. B 90 (2014), 085426.
[40] S. Cahangirov, V.O. Özcelik, L. Xian, J. Avila, S. Cho, M.C. Asensio, S. Ciraci, A. Rubio, Phys. Rev. B 90 (2014), 035448.
[41] F. Matusalem, M. Marques, L.K. Teles, F. Bechstedt, Phys. Rev. B 92 (2015), 045436.
[42] H. Wu, Y. Qian, Z. Du, R. Zhu, E. Kan, K. Deng, Phys. Lett.A 381 (44) (2017) 3754.
[43] Z. Zhou, X. Wu, J. Yang, Nanoscale 10 (2018) 1265.
[44] M. Qiao, Y. Wang, Y. Li, Z. Chen, J. Phys. Chem. C 121 (2017) 9627.
[45] Z. Wang, M. Zhao, X.F. Zhou, Q. Zhu, X. Zhang, H. Dong, A.R. Oganov, S. He, P. Grúnberg. http://arxiv.org/abs/1511.08848, 2015.
[46] H. Wu, Y. Qian, S. Lu, E. Kan, R. Lu, K. Deng, H. Wanga, Y. Ma, Phys. Chem. Chem. Phys. 17 (2015), 15694.
[47] H. Tu, J. Zhang, Z. Guo, C. Xu, RSC Adv. 9 (2019), 42245.
[48] P. Giannozzi, et al., J. Phys. Condens. Matter 21 (2009), 395502.
[49] P. Giannozzi, et al., J. Phys. Condens. Matter 29 (2017), 465901.
[50] J.P. Perdew, K. Burke, M. Ernzerhof, Phys. Rev. Lett. 77 (1996) 3865.
[51] P.E. Blöchl, Phys. Rev. B 50 (1994) 17953.
[52] A. Dal Corso, Comput. Mater. Sci. 95 (2014) 337.
[53] H.J. Monkhorst, D.J. Pack, Phys. Rev. B 13 (1976) 5188.
[54] S. Zhang, J. Zhou, Q. Wang, X. Chen, Y. Kawazoe, P. Jena, Proc. Natl. Acad. Sci. Unit. States Am. 112 (8) (2015) 2372.
[55] R. Qin, C.H. Wang, W. Zhu, Y. Zhang, AIP Adv. 2 (2012), 022159.
[56] R. Majidi, Theor. Chem. Acc 136 (2017) 109.
[57] M. Asadpour, S. Malakpour, M. Faghihnasiri, B. Taghipour, Solid State Commun. 212 (2015) 45.
[58] C.C. Liu, H. Jiang, Y. Yao, Phys. Rev. B 84 (2011), 195430.
[59] V.M. Pereira, A.H. Castro Neto, N.M.R. Peres, Phys. Rev. B 80 (2009), 045401.
[60] Y. Li, X. Jiang, Z. Liu, Z. Liu, Nano Res 3 (2010) 545.
[61] A. Bandyopadhyay, A. Nandy, A. Chakrabarti, D. Jana, Phys. Chem. Chem. Phys. 19 (2017), 21584.
[62] M. Zhou, R. Li, J. Zhou, X. Guo, B. Liu, Z. Zhang, E. Xiea, J. Appl. Phys. 106 (2009), 124315.